Journal of Molecular Liquids xxx (xxxx) 124583

Contents lists available at ScienceDirect

Journal of Molecular Liquids

journal homepage: www.elsevier.com/locate/molliq

Low-temperature and high-pressure phase transitions of ionic liquid 1-decyl-3-methylimidazolium bromide

Hiroshi Abe [a,*], Shusei Maruyama [a], Yuto Yoshiichi [a], Hiroaki Kishimura [a], Daisuke Okuyama [b], Hajime Sagayama [b]

[a] Department of Materials Science and Engineering, National Defense Academy, Yokosuka 239-8686, Japan
[b] Institute of Materials Structure Science, High Energy Accelerator Research Organization (KEK), Tsukuba 305-0801, Japan

ARTICLE INFO

Keywords:
Ionic liquids
Crystal polymorphs
Hybrid layered structure
Double Bragg reflection
Large bulk modulus

ABSTRACT

The phase behavior of an ionic liquid (IL) was investigated at low temperature (LT) and high pressure (HP). The utilized IL was 1-decyl-3-methylimidazolium bromide ([C_{10}mim][Br]), whose cation possesses a long alkyl side-chain. The LT- and HP-crystal polymorphs of [C_{10}mim][Br] were observed conducting small- and wide-angle X-ray scattering (SWAXS) experiments. Upon cooling, a liquid crystal was formed, which subsequently transformed into crystalline species with the modulated layered structure possessing the double Bragg reflection. In addition to the layered structure, the hybrid layered structure coexisted upon heating. At HP, 00ℓ Bragg reflections representing the layered structure were not observed in SWAXS patterns. The HP-crystal phase of [C_{10}mim][Br] was characterized by double Bragg reflection in the low scattering wavevector region. The non-layered HP-crystal caused the large bulk modulus.

1. Introduction

Ionic liquids (ILs) consisting of a cation and an anion have been utilized in various fields [1-10]. The representative cations of ILs are members of the 1-alkyl-3-methylimidazolium ([$C_n$mim]$^+$) ion family, where n indicates the alkyl side-chain length. The unique properties of ILs descend from their nano-heterogeneity [11-14]. The nano-heterogeneities of [$C_n$mim][Cl] (n = 3, 4, 6, 8, and 10) have previously been identified experimentally by conducting small-angle and wide-angle X-ray scattering (SWAXS) measurements [15]. Prepeak on the SWAXS patterns shifted to a lower Q value as the alkyl side-chain length increased. A [$C_n$mim]$^+$ cation with a long alkyl side-chain caused the liquid crystal (LC) phase at low temperature (LT) and ambient pressure [16-18]. A sharp Bragg reflection of the LC phase at Q_{LC} appeared at the prepeak position in the liquid state.

The molecular conformations of the [$C_n$mim]$^+$ cations have been investigated by performing Raman spectroscopy experiments in combination with density functional theory (DFT) calculations [19]. Based on the DFT-identified Raman bands, we can predict the local structures of the ILs with stable conformations. Conformational degrees of freedom indicate molecular flexibility, and ion pairing relating with molecular packing efficiency. The conformers, flexibility, and molecular packing influence a phase variety. According to the results of DFT calculations, the number and characteristics of the stable conformers of asymmetric [$C_n$mim]$^+$ cations varied depending on the alkyl side-chain length [20]. For instance, three stable conformers of [C_8mim]$^+$ were calculated to exist by DFT [21]. Experimentally, the Raman bands of [$C_n$mim][PFBS] (n = 4, 6, and 8) were obtained at LT [22] ([PFBS]$^-$: perfluorobutanesulfonate ion). The characteristics of the complex LT-crystal polymorphs were investigated conducting simultaneous SWAXS and differential scanning calorimetry (DSC) measurements. Relating to the LT-crystal polymorphs of [$C_n$mim][PFBS] [23], the cationic and anionic conformers changed subsequently [22]. In the case of [C_8mim][PFBS], the *trans*-based conformers were preferred to the *cis*-based conformers due to their superior molecular packing efficiency at LT. At high pressure (HP) and ambient temperature, HP-crystal polymorph, which is different from LT-crystal polymorph, occurred in [C_4mim][PFBS] [24]. The results of HP-Raman spectroscopy indicated that, as the pressure increased, the proportion of the *gauche* conformer of [C_4mim]$^+$ increased in the unit cells. In addition to the HP-crystal polymorphs, HP-multiple pathways of the phase transitions in [C_6mim][PFBS] appeared as an intrinsic property [25]. The 001 Bragg reflection at Q_{001} of [C_6mim][PFBS] was observed to be located in the lower Q region of Q_{LC}. The 00ℓ Bragg reflections at $Q_{00\ell}$ in the SWAXS pattern of HP-[C_6mim][PFBS] indicated that the sample was characterized by a hybrid layered structure, which is different from the stacking sequence

* Corresponding author.
E-mail address: ab@nda.ac.jp (H. Abe).

https://doi.org/10.1016/j.molliq.2024.124583
Received 9 October 2023; Received in revised form 20 February 2024; Accepted 26 March 2024
0167-7322/

of LC-based layered structure. Moreover, a hybrid layered structure was also induced in HP-[C_{10}mim][Cl] [26]. By contrast, at LT and ambient presure, the LC-based layered structure was found to be preferred by LT-[C_{10}mim][Cl], as made evident by the results of simultaneous SWAXS and DSC measurements. More interestingly, a hybrid layered structure was formed even at LT [27,28]. In contrast, HP-[C_{10}mim][NO_3] possessed the layered structures and the small bulk modulus [28].

In the present study, the LT- and HP-phase behaviors of [C_{10}mim][Br] were determined based on the results of SWAXS experiments. Upon cooling, the modulated layered structure having the double Bragg reflection, was observed. The hybrid layered structure was induced upon heating. By a rapid scan, a relationship between the double Bragg reflection-driven layered structure and the hybrid layered structure was clarified. In the HP-phase transitions at ambient temperature, non-layered structures possessing the double Bragg reflection were determined to appear, following both the compression and decompression processes. Under HP, the large bulk modulus of [C_{10}mim][Br] was derived from the non-layered structure.

2. Materials and methods

The IL, [C_{10}mim][Br] (IoLiTec GmbH, Germany), was used in this study. Due to high viscosity of [C_{10}mim][Br], water impurity was not examined using Karl Fischer titration. Thus, the purity was estimated using the van't Hoff equation [29]. The heat fusion (J/mol) was obtained using simultaneous LT-(SWAXS + DSC) measurements. The as-received samples were vacuum dried at 80 °C using a diaphragm vacuum pump (DTU-20, Ulvac Co.). By changing the vacuum drying time, the purity of the samples were obtained (Fig. S1). We collected data using the vacuum dried sample (24 h and 80 °C). Since the IL is hydrophilic, the sample was prepared in a dry box filled with dry helium gas so as to perform the LT experiments at ambient pressure. For the HP experiments, the sample was placed into a diamond anvil cell (DAC) inside a glove bag under a flow of dry helium gas.

Powder X-ray diffraction using a high-speed spinner was performed to remove the typical preferred orientation of the Debye rings on the BL-8B beamline of the Photon Factory at the High-Energy Accelerator Research Organization (KEK) in Japan. Two-dimensional (2D) diffraction patterns were obtained using PILATUS 3 S 1 M (DECTRIS Ltd.) [30], where the pixel size is 172 μm × 172 μm, and the detector area is 83.8 mm × 33.5 mm. Subsequently, the 2D data were converted to 1D intensity data to minimize the preferred orientation on the Debye rings. By a combination of the 2D detector and synchrotron radiation, the rapid scan was feasible, and hidden information was extracted. The liquid sample was put into the quartz capillary, whose diameter was 0.5 mm. The cooling system used was GN2-SN (Rigaku Co.). Since the K-edge of Br is 0.09199 nm, an incident wavelength of $\lambda = 0.094644$ nm was selected. The incident wavelength and the scattering angle, 2θ, were calibrated using a CeO_2 polycrystalline standard. The scattered wavevector, Q, is provided as $4\pi\sin(\theta)/\lambda$ (nm^{-1}). Using a small beam stop, the minimum Q (Q_{min}) was 1.16 nm^{-1}.

A Mao-Bell type DAC was used to conduct the HP-SWAXS experiments. The sample and ruby balls were loaded into the 0.35 mm hole of a pre-indented stainless-steel gasket, which was 0.15 mm thick. HP-SWAXS experiments were conducted on the BL-18C beamline of the Photon Factory, KEK [31,32]. 2D diffraction patterns were obtained using an imaging plate (IP) system (BAS2500, Fuji-Film Co., Japan) [31,32]. The IP was a digital X-ray film. In the center of the IP, the 2 mmϕ hole was punched to pass the incident X-ray (Fig. S2 (a) and (b)) [32]. The intensity of incident X-ray was monitored directly using an ion chamber. The scattered intensity was measured without using a direct beam stop. Q_{min} was 0.71 nm^{-1}. In order to eliminate air scattering, a vacuum chamber with polyimide (Kapton)-film windows was used (125 μm thickness). An incident microbeam was obtained using a double collimator system, wherein the diameter of the first collimator was 35 μm and that of the second collimator was 130 μm. Pressure was determined from the spectral shift of the R_1 fluorescent line of the ruby balls in the DAC. The incident wavelength was 0.09424 nm. λ and 2θ were calibrated using a CeO_2 polycrystalline standard.

The observed powder diffraction patterns were analyzed using *CONOGRAPH* software [33] and the *ab initio* structure determination program in *FOX* [34]. *CONOGRAPH* afforded the determination of the crystal system, while the lattice parameters and the molecular arrangements in the unit cell were simulated using *FOX*, which relies on global optimization algorithms.

3. Results and discussion

3.1. LT behavior of [C_{10}mim][Br]

In Fig. 1 (a) and (b), SWAXS experiments are conducted at ambient pressure that provide information on the LT phase behavior of [C_{10}mim][Br]. Given the large value of the X-ray atomic scattering factor of ^{35}Br, only information on ^{35}Br in [C_{10}mim][Br] is enhanced in the SWAXS patterns. The applied cooling and heating rates were 3 and 5 °C/min, respectively. At room temperature, [C_{10}mim][Br] was in the liquid (L) phase, and the prepeak was observed at 2.36 nm^{-1} (Fig. 2). Upon cooling, the LC phase appeared at −10.5 °C (T_{LC}) (Fig. 1(a)). In the SWAXS pattern revealed by the red curves, a sharp Bragg reflection was observed at $Q_{LC} = 2.30$ nm^{-1} (Fig. 2), whose location was close to the position of the prepeak in the L phase. In a previous study [35], the imidazolium-based LCs were synthesized, and sharp Bragg reflections appeared in the center of the prepeak position. By further cooling, the LC phase of [C_{10}mim][Br] was transformed into the crystal (C_I') phase, as was evinced from the specific double Bragg reflection at − 42.9 °C (T_{C1}). The C_I' phase was represented by the blue curves in Fig. 1(a). The SWAXS pattern was characterized by the double Bragg reflection at low Q region and the LC-like layered structure (Fig. 2). The peak positions of the double Bragg reflection were found to be 2.21 nm^{-1} (Q_1) and 2.39 nm^{-1} (Q_2). If we assume that the Q_2 peak corresponds to 001 Bragg reflection of the LC-like layered structure, the 00ℓ Bragg reflections indicated by the blue circles in Fig. 2 are assigned systematically. Therefore, the Q_1 peak of the double Bragg reflection could cause the lattice modulation of the LC-like layered structure. With decreasing temperature, the Q_2 peak increased gradually. Below − 50 °C, the Q_2 peak became almost constant. The crystal structure of the C_I' phase was determined to be monoclinic having long lattice constants (Table 1). The density (ρ) of the L phase at room temperature was 1.128 g/cm^3 [36]. The calculated ρ of the C_I' phase was 1.189 g/cm^3, a value only slightly larger than that of the L phase. Even as the temperature was made to decrease to the minimum temperature (T_{min} = − 100 °C) in the thermal cycle, the C_I' phase existed. Therefore, structure analysis was performed using the SWAXS pattern recorded at T_{min} (Fig. 3(a)). Consequently, upon cooling, the LT-crystal polymorph is characterized by the L–LC–C_I' phase transitions. Upon heating, the C_I' phase existed from T_{min} to − 50 °C (Fig. 1(b)). Above − 50 °C, the Q_1 peak became smaller, while the Q_2 peak intensity increased drastically. This means that the modulated effect was weakened, accompanied with increasing temperature. The green curves in Fig. 1(b) indicate that only double Bragg reflections changed distinctly on the SWAXS patterns. At − 6.5 °C (T_{C2}), the Q_1 peak vanished completely and the additional Bragg reflections appeared. The disappearance of the Q_1 peak implies that the C_I' phase became the non-modulated LC-like structure (C_I) just below T_{C2}. Using the SWAXS pattern at − 18.6 °C ($< T_{C2}$) in Fig. 3(b), we resolved the crystal structure of the non-modulated C_I phase, whose space group was orthorhombic. The crystal structural parameters of the C_I phase are listed in Table 1. Considering the drastic change on the SWAXS pattern, a crystal–crystal phase transition was observed to be induced at T_{C2}. Here, the new phase is named C_{II}. It is noteworthy that the lowest peak

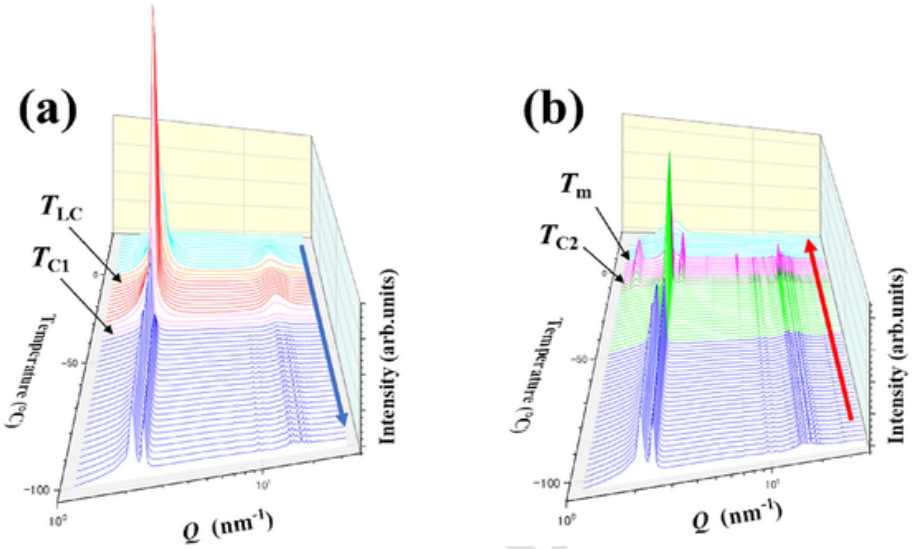

Fig. 1. Results of small- and wide-angle X-ray scattering (SWAXS) measurements conducted on [C_{10}mim][Br] upon (a) cooling and (b) heating. The labels "T_{LC}" and "T_{C1}" indicate the liquid (L)–liquid crystal (LC) phase transition temperature and LC–crystal (C_I) phase transition temperature observed upon cooling, respectively. T_{C2} and T_m indicate the temperature of the crystal 1 (C_I)–crystal 2 (C_{II}) phase transition and the melting point observed upon heating, respectively.

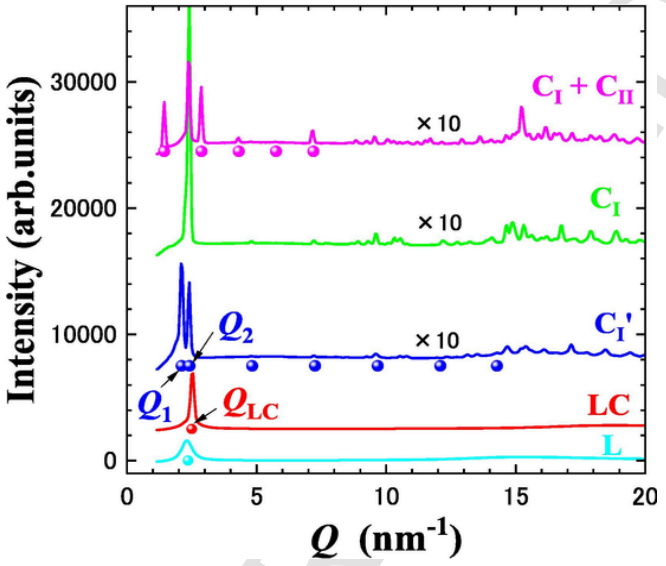

Fig. 2. Small- and wide-angle X-ray scattering (SWAXS) patterns obtained for [C_{10}mim][Br] at low temperature. L, LC, C_I', C_I, and C_{II} indicate the liquid, liquid crystal, modulated crystal 1, crystal 1, and crystal 2 phases, respectively. The double Bragg reflection of the C_I' phase appeared at Q_1 and Q_2. Q_{LC} denotes the peak position of the LC phase. The SWAXS patterns of C_I', C_I, and C_I + C_{II} are plotted by 10 times magnified intensities.

of the C_{II} phase located at 1.43 nm^{-1}, which was lower than the Q_1 position (Fig. 2). Thus, the C_{II} phase is regarded as the hybrid layered structure in the same manner with LT-[C_{10}mim][NO_3] [28]. Here, the presence of a hybrid layered structure is considered to be confirmed if the following observations are made: (i) the lowest Q of Bragg reflection is lower than Q_{LC}, and (ii) the 00ℓ Bragg reflections representing the layered structure. In fact, the Bragg reflections of the C_{II} phase at low Q region are explained by the 00ℓ Bragg reflections indicated by the purple closed circles in Fig. 2. Compared with the SWAXS patterns (Fig. 2), we deduce that the non-modulated C_I phase and C_{II} phases coexisted above T_{C2}. Due to the coexistence of the C_I and C_{II} phases, the hybrid layered structure of the C_{II} phase was not obtained by the structure analysis. Finally, the C_I and C_{II} phases were observed to disappear at 7.6 °C (T_m), concomitantly with the disappearance of the Bragg reflections. The complicated phase changes upon heating are summarized as C_I' → C_I → C_I + C_{II}. Here, we emphasize that in LT-[C_{10}mim][Br], the layered structures were preferred in the C_I', C_I, and C_{II} phases in spite of different stacking sequences.

3.2. HP behavior of [C_{10}mim][Br]

Generally, under HP conditions, molecular packing efficiency is the main factor determining a sample's crystal structure. The hybrid layered structure of HP-[C_{10}mim][Cl] [26] consisted of a folding layer (the *gauche*-like conformer) and a stacking layer (the *trans*-like conformer). The former is regarded as the glass-forming factor, while the latter is derived from the high molecular packing efficiency.

The halogen anion effect on the HP-crystal structure was investigated by HP-SWAXS at ambient temperature. Since the HP-phase behaviors of [C_{10}mim][Cl] have been investigated [26], the HP-SWAXS patterns in [C_{10}mim][Br] were collected to clarify the anion effect (Fig. 4(a) and (b)). The black and red curves represent the observed and calculated SWAXS patterns, respectively. Upon compression, crystallization of [C_{10}mim][Br] was observed to occur at 0.2 GPa (P_{C1}) in Fig. 4 (a). The obtained crystalline phase was named the α phase. The ideal Debye rings of the α phase were obtained in the IP (Fig. S2(a)). The 00ℓ Bragg reflections were not observed in the α phase of [C_{10}mim][Br]. Hence, HP-[C_{10}mim][Br] was not characterized by a layered structure. More importantly, a double peak appeared at low-Q values in the case of the HP α phase (Fig. 4(a)). The double-peak positions were 2.90 nm^{-1} (Q_1) and 3.11 nm^{-1} (Q_2), which meant that this peak appeared at higher Q values than the prepeak recorded for the L phase. Considering that no 00ℓ Bragg reflections were present and that the double peak appeared at low-Q values, the HP-crystal structure of [C_{10}mim][Br] was determined to be different from LT-crystal structure of the C_I' phase. Furthermore, the double Bragg reflection of [C_{10}mim][NO_3] [28] did not coincide with that of the LT-C_I' and HP- α phases of [C_{10}mim][Br]. By structure analysis, the crystal structure of the α phase was determined to be monoclinic (C2/m) in Table 1. The long lattice constants in Table 1 can explain the double peak at low-Q values. The fact that the α phase did not exhibit a layered structure

Table 1
Crystallographic data of [C_{10}mim][Br].

T (°C)		a (nm)	b (nm)	c (nm)	α	β	γ	Z	ρ (g/cm^3)	$_wR$ (%)	R (%)
−100 (C_I')	C2/m	2.4280	4.4212	1.9285	90	111.432	90	46	1.202	13.1	16.0
−18.6 (C_I)	Pmm2	1.4261	2.2142	2.6997	90	90	90	20	1.181	14.6	13.6
P (GPa)		a (nm)	b (nm)	c (nm)	α	β	γ	Z	ρ (g/cm^3)	$_wR$ (%)	R (%)
0.2	C2/m	2.4286	4.3430	1.8924	90	109.97	90	46	1.235	6.38	5.92
0.8	C2/m	2.4086	4.3424	1.9036	90	110.06	90	46	1.239	8.08	7.36
1.6	C2/m	2.3742	4.3336	1.9336	90	111.18	90	46	1.249	8.46	8.53
2.3	C2/m	2.3681	4.3270	1.9377	90	111.51	90	46	1.254	6.76	7.10
4.0	C2/m	2.3602	4.3306	1.9366	90	111.98	90	46	1.262	5.53	6.06
5.1	C2/m	2.3573	4.3134	1.9308	90	113.20	90	46	1.284	7.43	8.03
6.0	P2/m	0.5712	1.9104	2.1315	90	95.088	90	6	1.304	6.73	7.05
6.8	P2/m	0.5691	1.9101	2.1300	90	95.09	90	6	1.310	7.39	7.84
7.6	P2/m	0.5687	1.9101	2.1253	90	95.27	90	6	1.314	8.51	9.17
4.6	P2/m	0.5711	1.9126	2.1351	90	95.33	90	6	1.301	7.62	7.45
3.3	P2/m	0.5680	1.9344	2.1561	90	94.71	90	6	1.280	8.63	7.51
0.5	C2/m	2.3868	4.2646	1.8890	90	110.52	90	46	1.286	6.20	5.30

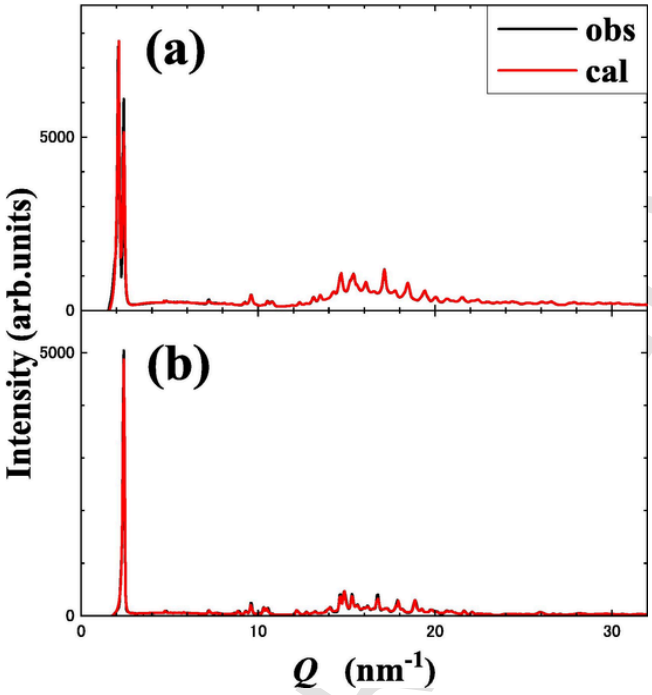

Fig. 3. Small- and wide-angle X-ray scattering (SWAXS) of the C_I' and C_I phases. The black and red curves indicate the observed and calculated SWAXS patterns of the C_I' and C_I phase, respectively. The crystal structure of the C_{II} phase was not resolved due to the two-phase coexistence.

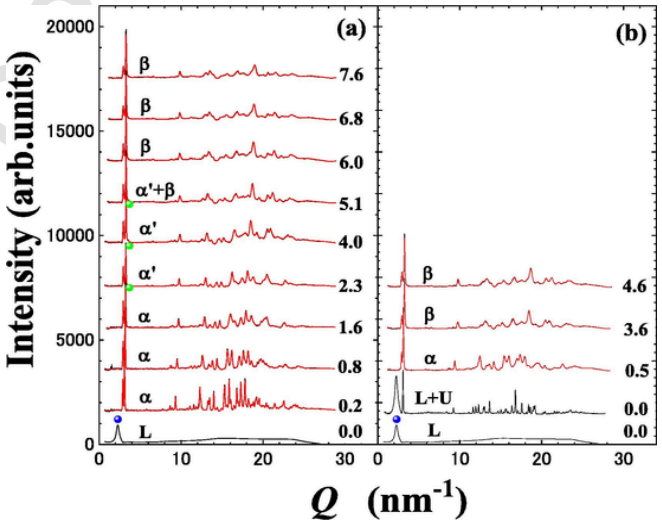

Fig. 4. Small- and wide-angle X-ray scattering (SWAXS) patterns obtained for [C_{10}mim][Br] upon (a) compression and (b) decompression. L and U indicate the liquid phase and an unknown crystal phase, respectively. The blue closed circles and green closed circles indicate the prepeak position in the SWAXS pattern of the L phase and the weak side-peak position in the α' phase, respectively.

could be supported by a lack of the 00ℓ Bragg reflections. As the pressure increased, the β angle of the monoclinic structure increased in value (Table 1). At 1.6 GPa, peak broadening became predominant in the high Q region, although the double peak at low Q was still sharp. At 2.3 GPa, the intensity ratio of the double peak changed. Indeed, the intensity of the Q_1 peak decreased substantially. The decrease of the Q_1 peak indicates the reduced modulation as well as the LT-C_I' phase. Moreover, a weak side-peak denoted by the closed green circle in Fig. 4 (a) appeared. This side-peak could be due to cationic conformational changes taking place. Since the atomic scattering factor of $[C_{10}mim]^+$ is quite small compared with that of ^{35}Br, cation changes only make a slight contribution to the Bragg intensity. Since the lattice parameters of the sample thus obtained were almost the same as those of the α phase (Table 1), the modulated lattice obtained at a 2.3 GPa value for the pressure was called the α' phase. As the sample was further compressed up to 6.0 GPa (P_{C2}), the side-peak disappeared. Additionally, the peak splitting of the double peak increased in size. Based on structure analysis, a new crystalline phase (dubbed β phase) was determined to form at P_{C2}. The crystal structure of the β phase was monoclinic (P2/m) in Table 1. Notably, at 5.1 GPa, the α and β phases coexisted, because the observed SWAXS pattern was fitted by both crystal structure models. The β phase was determined to be characterized by a smaller unit cell and a smaller β angle size than the α phase. The maximum pressure (P_{max}) applied in this study was 7.6 GPa. Even at P_{max}, the Q_2 component of the double peak was sharp, and the weak and broad Q_1 peak still existed.

Fig. 4(b) represents SWAXS patterns recorded during the decompression process. At 4.6 GPa, the lattice constants increased in value (Table 1), although the crystal structure of the sample was the same as that observed at P_{max}. Further decompression at 3.6 GPa resulted in the peak splitting of the double peak to become narrower. Indeed, as the pressure decreased from 4.6 GPa to 3.6 GPa, the characteristics of the crystal structure did not vary at all. Below 2 GPa, the pressure of the DAC immediately decreased. Using an optical microscope, a drastic change in crystal morphology was observed at 0.5 GPa. At this value for the pressure, moreover, the SWAXS patterns also changed (Fig. 4

(b)). By structure analysis, it was found that, at 0.5 GPa, the β phase returned to the α phase (Table 1). As the pressure decreased further, on the way to the melting process, a new crystal phase and liquid phase coexisted at 0.0 GPa. In addition to the prepeak, a preferred orientation on the Debye rings was detected (Fig. S2(b)). Thus, the crystal structure of the new phase was not resolved. The unknown phase was denoted by U (Fig. 4(b)). Finally, the sample melted completely at ambient pressure. During the HP cycle, a series of reversible phase transitions were observed in $[C_{10}mim][Br]$.

High pressure compression behavior has been analyzed using the second-order Birch-Murnaghan (BM) equation [37]. The second-order BM equation is provided by,

$$P = \frac{3}{2}K\left\{\left(\frac{V_0}{V}\right)^{\frac{7}{3}} - \left(\frac{V_0}{V}\right)^{\frac{5}{3}}\right\} \quad (1)$$

where K is the isothermal bulk modulus. In fact, K of $[C_{10}mim][NO_3]$ was estimated using the second-order BM equation [28]. K of $[C_{10}mim][NO_3]$ at low pressure region was 20 GPa, which was comparable to that of the flexible metal–organic frameworks. However, at high pressure region, K increased up to 50 GPa [28]. HP hardening occurred in $[C_{10}mim][NO_3]$. In case of $[C_{10}mim][Br]$, the entirely opposite behavior was observed (Fig. 5). Below P_{C2}, K of $[C_{10}mim][Br]$ was found approximately to be 150 GPa. Inversely, K decreased to 100 GPa above P_{C2}. With increasing pressure, HP softening was obviously observed in $[C_{10}mim][Br]$, even though the K values were larger than those of $[C_{10}mim][NO_3]$. Considering the common $[C_{10}mim]^+$ cation, the anion species caused the different compression behaviors.

3.3. Crystal structural analysis of the LT and HP phases

The crystal structures of $[C_2mim][Br]$ [38] and $[C_4mim][Br]$ [39] were determined by conducting single-crystal X-ray structural analyses. The space group of LT-$[C_2mim][Br]$ was $P2_1/c$ (monoclinic), while that of LT-$[C_4mim][Br]$ was $Pna2_1$ (orthorhombic). The lattice constants for both crystals did not exceed 2 nm. For instance, the unit cell of $[C_4mim][Br]$ is reported in Fig. 6(a) [39]. The crystal structures both of $[C_2mim][Br]$ and $[C_4mim][Br]$ indicate the presence of a 3D network of the cation and anion in the unit cells. Generally, the ability of a molecular system to exhibit 2D structural characteristics is determined by the stacking sequence [40]. As a result of competitive interactions and changes in the length of the alkyl chains of the ILs, LT-crystal polymorphs exhibiting various stacking sequences were produced at LT. Focusing on $[C_n mim][NO_3]$, the presence of 2D networks in the L, LC, and crystal phases, including the metastable phases, were demonstrated by the results of molecular dynamics simulations [41,42]. Moreover, two-step transitions were demonstrated in the simulation box. Particularly in $[C_{10}mim][NO_3]$, it was found that the HP-layered structure contributes to the small bulk modulus [28].

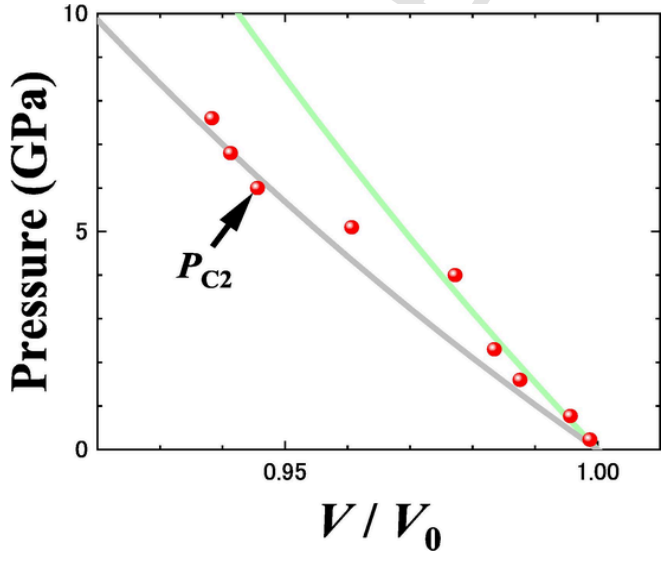

Fig. 5. Pressure increment by the isothermal bulk modulus. Two solid curves are calculated using second-order Birch–Murnaghan equation. The grey and green curves were calculated using bulk moduli of 100 GPa and 150 GPa, respectively.

In the case of $[C_{10}mim][Br]$, the LT-crystal structure of the modulated C_I' phase is reported in Fig. 6(b). The $[C_{10}mim]^+$ cations are omitted in the unit cell due to small atomic scattering factors of the cations. The *trans* and *gauche* conformers of $[C_{10}mim]^+$ and orientational order were not clarified in this study. The LT layered structure is expressed by the 2D arrangement of Br, and the visualized unit cell was calculated by the occupation probability of Br of 0.5. The double Bragg reflection and 00ℓ Bragg reflections of the C_I' phase reported in Fig. 2 reflected the large size of the unit cell, reflecting the modulated stacking sequence. Further, the non-modulated lattice of the C_I phase without forming the double Bragg reflection is expressed as the smaller layered structure in Fig. 6(c), where the occupation probability of Br is 0.5 (Fig. 6(c)). On the other hand, under HP conditions, a 3D network of Br atoms developed in the α phase upon compression (Fig. 6(d)). At 0.2 GPa, the sharp Bragg reflections observed in the SWAXS pattern reported in Fig. 4(a) indicate that the α phase is characterized by a high level of crystallinity. The large size of the unit cell of the α phase, which is reflected by the data listed in Table 1, provides the low-Q double peak. Generally, under HP, the ILs have been observed to be characterized by layered structures (Table 2) [25-28]. However, in the case of HP-$[C_{10}mim][Br]$, a non-layered structure was obviously realized relating with the large bulk modulus. Fig. 6(e) indicates the unit cell of the β phase at P_{max}. Obviously, the 3D network of the Br atoms was preserved at the mentioned pressure. Thus, under HP, the layered structure did not develop in $[C_{10}mim][Br]$. At 7.6 GPa, a low degree of crystallinity was obtained in the β phase due to lattice strain (Fig. 4(a)). We deduce that, at the specified pressure, *gauche*-like conformations of $[C_{10}mim]^+$ appear and orientational disorder is promoted. Since the equivalent lattice sites increased due to the orientational disorders, smaller unit cell of the β phase is reported in Fig. 6(d).

The double peak at low-Q values for LT- and HP-$[C_{10}mim][Br]$ was observed in this study for the first time. The layered and non-layered structures of the various ILs are reflected by the data listed in Table 2. Notably, $[C_{10}mim][Cl]$ and $[C_{10}mim][Br]$ were determined to belong to different space groups, in spite of the same halogen anions (X = Cl and Br). By contrast, the orthorhombic LT-$[C_4mim][Cl]$ and LT-$[C_4mim][Br]$ belonged to the same space group, and their lattice parameters were similar [38]. Hence, the length of the alkyl side-chains could contribute to $[C_{10}mim][Cl]$ and $[C_{10}mim][Br]$ being characterized by different crystal structures. In particular, the inherent crystallographic features of HP-$[C_{10}mim][Br]$ are its large unit cell and the absence of a layered structure. Here, under HP, the fact that a non-layered structure for the $[C_{10}mim]^+$-based ILs was observed for the first time in this study should be emphasized.

4. Conclusion

The LT- and HP-phase transitions of $[C_{10}mim][Br]$ were examined conducting SWAXS experiments. LT- and HP-crystal polymorphs were observed for $[C_{10}mim][Br]$. By a rapid scan, in LT-$[C_{10}mim][Br]$, the hidden phases such as the modulated LC-based layered and hybrid layered structures were extracted. The double Bragg reflection in the LC-like layered structure contributed the lattice modulation. On the other

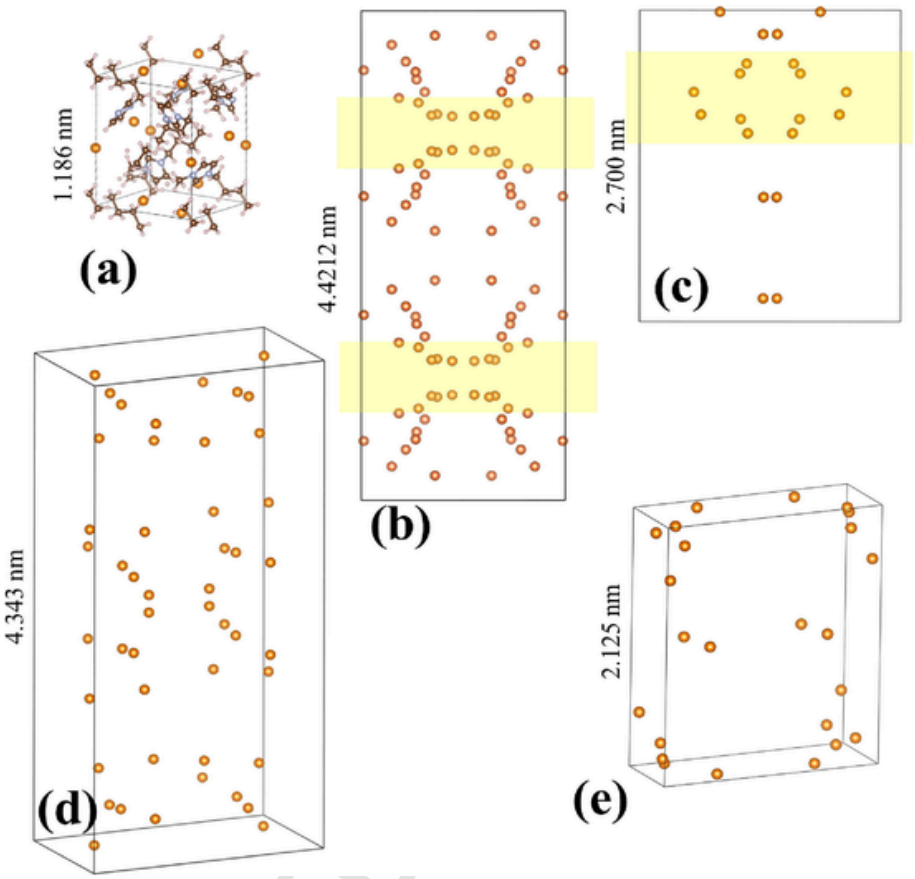

Fig. 6. Unit cells of (a) low-temperature (LT)-[C_4mim][Br] [36], (b) modulated crystal 1 (C_I') phase of LT-[C_{10}mim][Br], (c) crystal 1 (C_I) phase of LT-[C_{10}mim][Br], (d) α phase of high-pressure (HP)-[C_{10}mim][Br] (0.2 GPa), and (e) β phase of HP-[C_{10}mim][Br] (7.6 GPa).

Table 2
Classification of layered and non-layered structures of the various ionic liquids.

Layered (00ℓ Bragg reflections)		Non-layered (double peak)
LC-based layered	Hybrid-layered	3D network
	HP-[C_6mim][PFBS]	
LT-[C_{10}mim][Cl]	HP-[C_{10}mim][Cl]	
LT-[C_{10}mim][Br]	LT-[C_{10}mim][Br]	HP-[C_{10}mim][Br]
	LT-[C_{10}mim][NO_3]	
	HP-[C_{10}mim][NO_3]	HP-[C_{10}mim][NO_3]

hand, under HP conditions, the double peak also appeared at low-Q values in the SWAXS pattern, in the absence of the 00ℓ Bragg reflections. Based on the results of crystal structure analysis, HP-[C_{10}mim][Br] was determined to possess a large unit cell and to be characterized by a non-layered structure. The 3D network of HP-[C_{10}mim][Br] was connected with the large bulk modulus. Notably, the crystal structure of HP-[C_{10}mim][Br] was completely different from that of HP-[C_{10}mim][Cl].

CRediT authorship contribution statement

Hiroshi Abe: Conceptualization, Formal analysis, Writing – original draft, Writing – review & editing. **Shusei Maruyama:** Data curation. **Yuto Yoshiichi:** Data curation. **Hiroaki Kishimura:** Data curation. **Daisuke Okuyama:** Data curation. **Hajime Sagayama:** Data curation, Methodology.

Declaration of competing interest

The authors declare that they have no known competing financial interests or personal relationships that could have appeared to influence the work reported in this paper.

Data availability

Data will be made available on request.

Acknowledgements

We would like to thank Dr. T. Takekiyo and Prof. Y. Yoshimura of the National Defense Academy for the helpful discussions. We also thank the Photon Factory Program Advisory Committee (Proposal Nos: 2019G006, 2021G004, and 2022G556). *VESTA 3* was used for displaying crystal structures [43].

Appendix A. Supplementary material

Supplementary data to this article can be found online at https://doi.org/10.1016/j.molliq.2024.124583.

References

[1] N.V. Plechkova, K.R. Seddon, Applications of ionic liquids in the chemical industry, Chem. Soc. Rev. 37 (2008) 123–150.
[2] H. Wang, G. Gurau, R.D. Rogers, Ionic liquid processing of cellulose, Chem. Soc. Rev. 41 (2012) 1519–1537.
[3] Z. Lei, C. Dai, B. Chen, Gas solubility in ionic liquids, Chem. Rev. 114 (2014)

1289–1326.
[4] J. Wu, Z. Lan, J. Lin, M. Huang, Y. Huang, L. Fan, G. Luo, Electrolytes in dye-sensitized Solar cells, Chem. Rev. 115 (2015) 2136–2173.
[5] S. Zeng, X. Zhang, L. Bai, X. Zhang, H. Wang, J. Wang, D. Bao, M. Li, X. Liu, S. Zhang, Ionic-liquid-based CO_2 capture systems: structure, Interaction and process, Chem. Rev. 117 (2017) 9625–9673.
[6] S.P.M. Ventura, F.A. e Silva, M.V. Quental, D. Mondal, M.G. Freire, J.A.P. Coutinho, Ionic-liquid-mediated extraction and separation processes for bioactive compounds: past, present, and future trends, Chem. Rev. 117 (2017) 6984–7052.
[7] K.S. Egorova, E.G. Gordeev, V.P. Ananikov, Biological activity of ionic liquids and their application in Pharmaceutics and medicine, Chem. Rev. 117 (2017) 7132–7189.
[8] Y. Qiao, W. Ma, N. Theyssen, C. Chen, Z. Hou, Temperature-responsive ionic liquids: fundamental behaviors and catalytic applications, Chem. Rev. 117 (2017) 6881–6928.
[9] M. Watanabe, M.L. Thomas, S. Zhang, K. Ueno, T. Yasuda, K. Dokko, Application of ionic liquids to energy storage and conversion materials and Devices, Chem. Rev. 117 (2017) 7190–7239.
[10] J. Kadokawa, Application of ionic liquids for the functional materialization of chitin, Mater. Adv. 3 (2022) 3355–3364.
[11] T.L. Greaves, C.J. Drummond, Protic ionic liquids: evolving Structure–Property relationships and expanding applications, Chem. Rev. 115 (2015) 11379–11448.
[12] J.E.S.J. Reid, C.E.S. Bernardes, F. Agapito, F. Martins, S. Shimizu, M.E. Minas da Piedade, A.J. Walker, Structure–property relationships in protic ionic liquids: a study of solvent–solvent and solvent–solute interactions, Phys. Chem. Chem. Phys. 19 (2017) 28133–28138.
[13] J.M. Gomes, S.S. Silva, R.L. Reis, Biocompatible ionic liquids: fundamental behaviours and applications, Chem. Soc. Rev. 48 (2019) 4317–4335.
[14] H. Sadeghian, L. Maftoon-azad, T. Jalali, How ionic structure governs bulk properties: Charge lever moments of alicyclic ionic liquids utilized in lithium metal batteries, J. Electrochem. Soc. 169 (2022) 070521–*.
[15] A. Triolo, O. Russina, H.-J. Bleif, E.D. Cola, Nanoscale segregation in room temperature ionic liquids, J. Phys. Chem. B 111 (2007) 4641–4644.
[16] J.D. Holbrey, K.R. Seddon, Ionic liquids, Clean Prod. Proc. 1 (1999) 223–236.
[17] K. Goossens, P. Nockemann, K. Driesen, B. Goderis, C. Görller-Walrand, K.V. Hecke, L.V. Meervelt, E. Pouzet, K. Binnemans, T. Cardinaels, Imidazolium ionic liquid crystals with pendant mesogenic groups, Chem. Mater. 20 (2008) 157–168.
[18] K. Goossens, K. Lava, C.W. Bielawski, K. Binnemans, Ionic liquid crystals: versatile materials, Chem. Rev. 116 (2016) 4643–4807.
[19] V.H. Paschoal, L.F.O. Faria, M.C.C. Ribeiro, Vibrational spectroscopy of ionic liquids, Chem. Rev. 117 (2017) 7053–7112.
[20] T. Endo, T. Higuchi, Y. Kimura, DFT study on conformation of 1-Alkyl-3-methylimidazolium with ethyl, propyl, butyl, pentyl, and hexyl group, Bull. Chem. Soc. Jpn. 93 (2020) 720–729.
[21] S. Bilgili, F. Bardak, E. Kose, A. Atac, Investigation of the interionic interactions and spectroscopic features of 1-Octyl-3-methylimidazolium chloride, tetrafluoroborate, and hexafluorophosphate ionic liquids: an experimental survey and DFT modeling, J. Mol. Struct. 1261 (2022) 132912–132914.
[22] H. Abe, H. Kishimura, M. Uruichi, A phase variety of fluorinated ionic liquids: Molecular conformational and crystal polymorph, Spectrochim. Acta A 286 (2022) 121948.
[23] Y. Koyama, S. Shimono, H. Abe, K. Matsuishi, Crystal polymorphs in 1-alkyl-3-methylimidazolium perfluorobutanesulfonate ionic liquids, J. Mol. Liq. 317 (2020) 113908.
[24] Y. Koyama, S. Shimono, H. Kishimura, T. Takekiyo, Y. Yoshimura, H. Abe, K. Matsuishi, High-pressure crystal polymorphs in 1-butyl-3-methylimidazolium perfluorobutanesulfonate, J. Mol. Liq. 335 (2021) 116415–116417.
[25] H. Abe, Y. Koyama, S. Shimono, H. Kishimura, K. Matsuishi, High-pressure crystal polymorphs and multiple pathways in 1-hexyl-3-methylimidazolium perfluorobutanesulfonate ionic liquid, Chem. Phys. 557 (2022) 111479.
[26] H. Abe, N. Hamaya, Y. Koyama, H. Kishimura, T. Takekiyo, Y. Yoshimura, D. Wakabayashi, N. Funamori, K. Matsuishi, Long periodic structure of a room-temperature ionic liquid by high-pressure small-angle X-ray scattering and wide-angle X-ray scattering: 1-Decyl-3-methylimidazolium chloride, ChemPhysChem 19 (2018) 1441–1447.
[27] H. Abe, H. Kishimura, Multistep phase transition in 1-decyl-3-methylimidazolium nitrate ionic liquid, J. Mol. Liq. 352 (2022) 118695–118698.
[28] H. Abe, Y. Yoshiichi, H. Kishimura, H. Sagayama, Low-temperature and high-pressure phase transitions in 1-decyl-3-methylimidazolium nitrate ionic liquid, Chem. Phys. Lett. 827 (2023) 140685–140687.
[29] G.G.G. de Oliveira, A. Feitosa, K. Loureiro, A.R. Fernandes, E.B. Souto, P. Severino, Compatibility study of paracetamol, chlorpheniramine maleate and phenylephrine hydrochloride in physical mixtures, Saudi Pharm. J. 25 (2017) 99–103.
[30] Z. Huang, L. Li, T. Wu, T. Xue, W. Sun, Q. Pan, H. Wang, H. Xie, J. Chi, T. Han, X. Hu, M. Su, Y. Chen, Y. Song, Wearable perovskite solar cells by aligned liquid crystal elastomers, Nature Commun. 14 (2023) 1204–1211.
[31] O. Shimomura, K. Takemura, H. Fujihisa, Y. Fujii, Y. Ohishi, T. Kikegawa, Y. Amemiya, T. Matsushita, Application of an imaging plate to high-pressure x-ray study with a diamond anvil cell, Rev. Sci. Inst. 63 (1992) 967–973.
[32] T. Sato, N. Funamori, D. Wakabayashi, K. Nishida, T. Kikegawa, Coexistence of two states in optically homogeneous silica glass during the transformation in short-range order, Phys. Rev. B 98 (2018) 144111–144116.
[33] R. Oishi-Tomiyasu, Robust powder auto-indexing using many peaks, J. Appl. Cryst. 47 (2014) 593–598.
[34] V. Favre-Nicolin, R. ˇ Cerńy, *FOX*, 'free objects for crystallography': a modular approach to *ab initio* structure determination from powder diffraction, J. Appl. Cryst. 35 (2002) 734–743.
[35] P.H.J. Kouwer, T.M. Swager, Synthesis and mesomorphic properties of rigid-Core ionic liquid crystals, J. Am. Chem. Soc. 129 (2007) 14042–14052.
[36] J. Klomfar, M. Souc˘ková, J. Pátek, Experimental densities and surface tension and models generating the best-current-knowledge values of them for members of 1-c_n-3-methylimidazolium bromide homologous series, J. Chem. Thermodyn. 118 (2018) 225–234.
[37] T. Katsura, Y. Tange, A simple derivation of the birch-murnaghan equations of state (EOSs) and Comparison with EOSs derived from other definitions of finite strain, Minerals 9 (2019) 745.
[38] A. Elaiwi, P.B. Hitchcock, K.R. Seddon, N. Srinivasan, Y.-M. Tan, T. Welton, J.A. Zora, Hydrogen bonding in imidazolium salts and its implications for ambient-temperature Halogenoaluminate(lll) ionic liquids, J. Chem. Soc. Dalton Trans. 3467–3472 (1995).
[39] J.D. Holbrey, W.M. Reichert, M. Nieuwenhuyzen, S. Johnston, K.R. Seddon, R.D. Rogers, Crystal polymorphism in 1-butyl-3-methylimidazolium halides: supporting ionic liquid formation by inhibition of crystallization, Chem. Commun. 1636–1637 (2003).
[40] M. Gardon, C.B. Pinheiro, G. Chapuis, Structural phases of hexamethylenetetramine–pimelic acid (1/1): a unified description based on a stacking model, Acta Cryst. B 59 (2003) 527–536.
[41] W. Cao, Y. Wang, G. Saielli, Metastable state during melting and Solid–Solid phase transition of [CnMim][NO3] (n = 4–12) ionic liquids by Molecular dynamics simulation, J. Phys. Chem. B 122 (2018) 229–239.
[42] S. Li, Y. Wang, Percolation phase transition from ionic liquids to ionic liquid crystals, Sci. Rep. 9 (2019) 13169.
[43] K. Momma, F. Izumi, VESTA 3 for three-dimensional visualization of crystal, volumetric and morphology data, J. Appl. Cryst. 44 (2011) 1272–1276.